Prompt gamma energy integration: a new method for online-range verification in proton therapy with pulsed-beams

Pierre Everaere[1], Denis Dauvergne[1]*, Marie-Laure Gallin-Martel[1],
Joël Hérault[2], Ayoub Koudia[1], Charbel Koumeir[3,4],
Jean Michel Létang[5] and Étienne Testa[6]

[1]Université Grenoble Alpes, CNRS/IN2P3, Grenoble INP, LPSC, UMR 5821, Grenoble, France, [2]Centre
Antoine Lacassagne, Department of Radioncology, Nice, France, [3]GIP ARRONAX, Saint Herblain,
France, [4]IMT Atlantique, Nantes University, CNRS/IN2P3 UMR 6457, Subatech, Nantes, France, [5]INSA-
Lyon, Université Claude Bernard Lyon 1, UJM-Saint Étienne, Centre Léon Bérard, CNRS UMR 5220,
Inserm U1294, CREATIS, Lyon, France, [6]Université Claude Bernard Lyon 1, CNRS/IN2P3 UMR 5822, IP2I,
Villeurbanne, France

Introduction: We propose a method for prompt-gamma verification of proton range during particle therapy, called Prompt-Gamma Energy Integration (PGEI).

Method: This method is based on the measurement of the total energy deposited in a set of detectors located around a patient. It is particularly suited in the case of high-instantaneous beam intensities, like for pulsed beams extracted from a synchro-cyclotron. GATE simuations were used to evaluate the sensitivity, and dedicated scintillators were tested as a function of beam intensity.

Results and discussion: Simulations show that millimetric range shifts can be measured at a beam-spot scale. The sensitivity is slightly degraded as compared to the Prompt-Gamma Peak Integration Method, for which Time-of-Flight can be employed to reduce the background in single-photon detection conditions at cyclotron accelerators. Experimentally, lead tungstate scintillators have shown to cope with the high instantaneous gamma count rates for PGEI at synchro-cyclotrons.

KEYWORDS

prompt-gamma, particle therapy, range verification, Monte Carlo simulations, integral method

1 Introduction

In the field of cancer treatment using particle therapy, a crucial asset consists in the ballistic precision, associated to the energy concentration deposited by light ions at the end of their path (Bragg peak), with small lateral and longitudinal dispersions. This feature offers the advantage of fine-tuning treatment precision to the tumor while limiting the impact on surrounding healthy tissues. This can minimize the number of radiation fields needed, a particularly important factor when dealing with tumors close to vital organs [1]. However, various factors have an impact on the location of the Bragg peak, leading to potential sources of errors that might result in under-dosing the tumor or, conversely,

overdosing the healthy neighboring tissues. Therefore, additional safety margins are usually applied to account for range uncertainties, and treatment plannings are performed with multi-field plans without organ-at-risk downstream the Bragg peak [2, 3]. As a consequence, the online monitoring of ion ranges inside the patient is highly desirable in order to fully benefit from the ballistic properties of ions. Indeed, better confidence in ion ranges could allow the medical physicists to improve the treatment plans, with less irradiation fields, and possibly organs-at-risk downstream the tumor volume, hence reducing the volume of irradiated healthy tissue [2]. Currently, no method has been widespread in clinical routine, since it would require online imaging, that has to comply with the patient workflow, and be adapted to the accelerator and beam-delivery system.

Positron Emission Tomography (PET) is based on the detection of nuclear collision-induced positron annihilation. It has been widely investigated and tested in clinics [4–8]. However, this technique is limited by the lifetime of radioisotopes, the biological washout, and the available statistics. Therefore, it requires either dedicated online imaging systems, or long data acquisitions offline. In any case, real-time information on a spot-by-spot basis is not feasible. Since the early 2000s, other approaches have been investigated, with a focus on the detection of prompt-secondary particles, particularly the prompt gamma rays (PG), to set up real-time control [9]. The high correlation between the emission points of PG and the trajectories of primary ions has been demonstrated [10, 11]. Furthermore, the vast majority of PG are emitted within a few picoseconds after the interaction, with a roughly isotropic angular distribution, and PG energy spectra strongly depend on the target chemical composition [12, 13]. Various techniques for PG detection have been considered. These encompass imaging systems that use mechanical [14–16] or electronic collimation (such as Compton cameras [17–22], or high-resolution Time-of-Flight collimation, as seen in Prompt-Gamma Time Imaging [23, 24]). Non-imaging setups (Prompt-Gamma Timing [25], Prompt-Gamma Spectroscopy [12], Prompt-Gamma Peak Integration (PGPI) [26] and Coaxial Prompt Gamma-ray Monitoring (CPGM) [27]) have been also investigated. These techniques need to be compliant with the beam intensities in order to provide photon-per-photon detection and proton range information. In particular, high-resolution Time-of-Flight (ToF) measurements (projectile-per-projectile) requires reduced intensities with respect to clinical ones [28]. The challenge of adapting the PG detection system with clinical beam delivery has become very complex with the rise of synchrocyclotron accelerators (e.g., IBA-S2C2), with low duty cycle and high instantaneous intensities (from 100 nA to 1 µA) compared to cyclotrons which usually operate in the nanoampere range, although their average intensities are somewhat similar [29]. Moreover, recent developments in the FLASH therapy field underscore the shift toward higher-intensity treatments doled out over shorter time spans to amplify therapeutic advantages [30, 31].

Some techniques of ion-range verification based on the measurements of electric and magnetic fields induced by the beam particles [32, 33] and the secondary particles [34] could benefit from these high intensity beams. This is also the case for the detection of ionoacoustic waves generated when the ion bunches interact with the medium [35, 36]. To alleviate the instrumentation constraints of the event-by-event detection in the context of high-intensity pulsed-beams, the present paper proposes a new method, named Prompt-Gamma Energy Integration (PGEI), derived from the PGPI. It consists in detecting all secondary radiation (mainly PG) with a set of a few detectors in "integration mode" (to cope with high particle fluxes). The information collected is the energy deposition of secondary particles during a beam pulse (integration mode obviously prevents ToF and PG energy measurements). This work consists of two independent and complementary simulation and experimental studies. In a first step, Monte Carlo simulations based on the open-source GATE software [37] are used to evaluate the potential of the method at spot scale. In a second step, we present preliminary measurements showing the feasibility to use fast- and low-luminosity scintillators in order to cope with high PG instantaneous fluxes.

2 Materials and methods

2.1 Simulations

2.1.1 Mean number of PG detected per HF period from a cyclotron and a synchrocyclotron

The PGPI method, proposed in [26], aims at providing ion-range verification from the PG count rates measured by a set of detectors placed around the patient. The count rates of each detector and their ratios, provide information on the beam range, that can be compared quantitatively to simulations. The number of secondary particles induced by nuclear collisions in the patient material is directly related to the intensity of the incident beam. Thus, when several PG interact in a single detector during the same incident particle bunch, there is a risk of information loss. Therefore, the PGPI method is effective when detection units present a compromise between detection efficiency (solid angle) and the probability to avoid pile-up. This compromise is optimum for a maximum duty cycle of the accelerator, e.g., with cyclotron-type accelerators that deliver a continuous beam with a current of the order of a few nA (example: IBA C230, average current 3 nA, HF period 10 ns [29]). However, in the context of using synchrocyclotron accelerators and their pulsed mode, a strong issue arises due to the peak intensity during beam delivery. For example, the IBA-S2C2 accelerator emits pulses with a duration of approximately 10 µs, spaced by about 1 ms, i.e., with a duty-cycle of 1%. These pulses themselves consist of a substructure with a period of 16 ns at the extraction, including 8 ns "on" periods delivering particle bunches and 8 ns "off" periods. Therefore, peak intensities may vary between 100 nA and 1 µA for averaged intensities of a few nA [29].

In order to determine the number of PG events detected per accelerator period (i.e., particle bunch), Monte Carlo simulations were performed with GATE (version 9.0) [37], a open-source software which is based on the Geant4 toolkit [38]. We used the QGSP_BIC_HP_EMZ physics list recognized as a reference in this field [39], since it includes both electro-magnetic physics (EMZ is a combination of the most accurate EM models) and hadronic physics. The simulation setup consisted in the 160 MeV proton irradiation of a spherical PMMA phantom target (density 1.2 g/cm^3) with a radius of 10 cm. Figure 1 shows the number of PG events detected per accelerator period as a function of the geometric
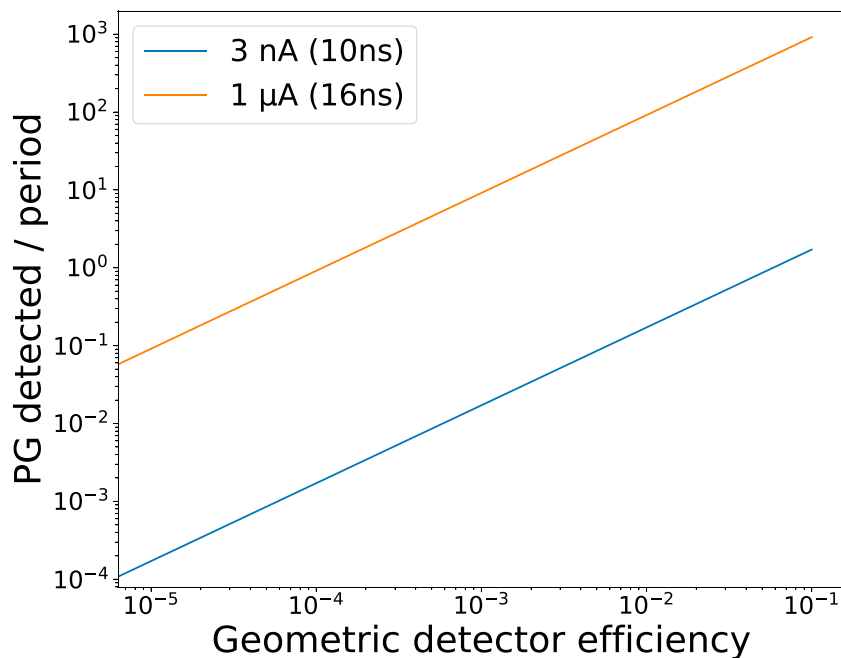
FIGURE 1
Mean number of PG detected per HF period (i.e., particle bunch) as a function of detector geometric efficiency during beam extraction of two accelerators: 1 µA peak current of a the IBA-S2C2 synchro-cyclotron with 16 ns period, and 3 nA average current of a the IBA-C230 cyclotron, with 10 ns period.
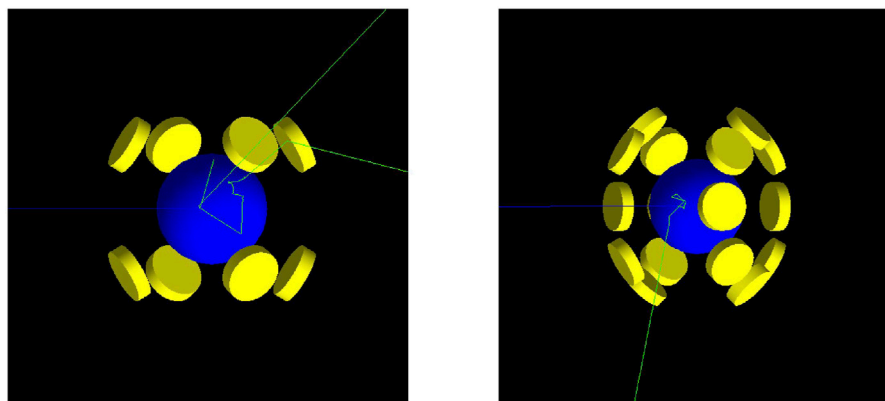
FIGURE 2
Geometries simulated in GATE: a spherical PMMA target (10-cm radius) placed at the center of the geometry surrounded by 8 (left) or 16 (right) LaBr$_3$ crystals with their entrance face at 20 cm from the target center.

efficiency of the detector. The values for both the IBA-S2C2 synchro-cyclotron and the IBA-C230 cyclotron, with similar average beam current (3 nA) are depicted on this graph. It is observed that the continuous beam of the C230 has the advantage of generating a low number of PG events per particle bunch. Therefore, it is possible to keep the geometric efficiency of the detector at the level of 10^{-3} while maintaining acceptable counting rates (around 1 MHz). In contrast, the low duty cycle, and thus the high intensities achieved by the S2C2, generate a much higher number of PG events per particle bunch, requiring a significantly reduced geometric detection efficiency (at the level

of 10^{-5}) for a single-photon detection regime. This limitation would result in a reduction of the size of the detection units, and then to a large increase of the number of detectors in order to preserve the statistical precision of the measurement.

2.1.2 Simulations of the PGPI and PGEI techniques

In order to address this issue and preserve the concept of a low-cost, simple arrangement of a few detection units, the proposed PGEI method relies on integral measurement of the energy deposited by secondary particles during the beam pulse in each detector placed around the patient. To determine the precision of this method and
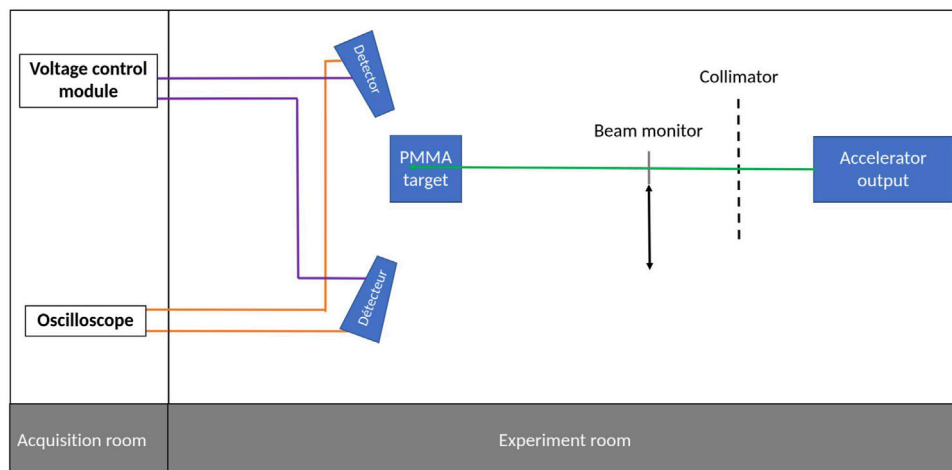
FIGURE 3
Experimental setup diagram.

compare it with the PGPI method, GATE simulations were performed. A sketch of the simulations is shown in Figure 2. A spherical PMMA target with a 10-cm radius was placed at the center of the geometry, surrounded by 8 or 16 LaBr$_3$ crystals with their entrance face at 20 cm from the target center. The choice of the LaBr$_3$ scintillation material has minor importance at this stage, since it is considered only as a calorimeter. Each of these crystals is a cylinder with a radius of 5 cm and a depth of 2.5 cm, corresponding to a geometric efficiency of approximately 1.5% relative to the simulation center. For each primary particle, the number of particles and the deposited energy in each detector ("sensitive detectors" in GATE) are recorded. The target was irradiated by a beam of 10^9 protons with an energy of 160 MeV. The beam-time structure was modeled in post-processing. Statistical fluctuations on the number of protons per bunch were applied following the Poisson distribution.

Multiple simulations are conducted with lateral (16-detector setup) or longitudinal (8-detector setup) displacements of the target relative to the proton beam direction, allowing the observation of the evolution of each variable (energy deposited or number of particles) as a function of the target position. A data analysis is employed to determine the number of particles detected within the detectors as well as their energy deposition. In the case of PGPI, we did not perform Time-of-Flight discrimination, in order to have the closest comparison with the PGEI method. However, a threshold of 1 MeV energy deposited was applied in order to discriminate PG from other secondary particles in the sensitive detectors. This threshold is the optimal value to reject most of electrons, low energy X-rays and a large fraction of Compton-scattered gamma, for which the correlation with emission vertex is poor. In practice, to increase the perceived statistics for an observable and improve the precision of the methods, it is possible to gather detectors into several groups for longitudinal displacement, thanks to their symmetrical positions relative to the emission points of secondary particles and the simple geometry used here. The results can then be compared on a reduced and more clinically relevant sample for 10^6, 10^7, and 10^8 incident protons to determine the sensitivity of the method in real conditions. Moreover, this

simulation makes it possible to estimate the flux of secondary particles and energy deposited in the detectors, providing insights for the design of a detection system.

2.2 Experiments

The method we used to characterize the detectors under a proton or alpha beam of ~70 MeV (total energy) is presented in Figure 3. These experiments took place at CAL-Nice and at ARRONAX-Saint-Herblain. Both accelerators are cyclotrons, and ARRONAX is equipped with a pulsation at injection, allowing the generation of a pulsed beam similar to that of a synchrocyclotron, with adjustable pulse and inter-pulse durations.

The detectors used in these experiments are scintillators coupled to photomultiplier tubes. Various scintillation crystals were employed to determine optimal characteristics based on their luminosity and scintillation constants.

A PMMA target serves as a phantom to stop the proton beam and generate secondary radiation. In the following, we will focus mainly on the results obtained at ARRONAX with pulsed beams, whereas experiments at CAL were used to study the behaviour of various detectors with continuous beams. The target was irradiated with a beam whose intensity could be adjusted up to 20 μA during pulses at ARRONAX. The measurement of the beam intensity was carried out by an ionization chamber located upstream from the exit window of the accelerator beamline in vacuum. Detectors are positioned around the target to detect the secondary radiation or particles produced during irradiation. The signals from the detectors are recorded using a LeCroy DSO oscilloscope, allowing automatic recording of approximately 100 waveforms of the characterized detector signals with 20 GHz sampling period. Recording is triggered by the beam pulse signal. Figure 4 provides an example of waveforms obtained on a PbWO$_4$ detector at ARRONAX, illustrating the correlation between the signal of the incident alpha beam pulse from a fast beam monitor (single diamond used as a solid-state ionization chamber) and the generated secondary particles.
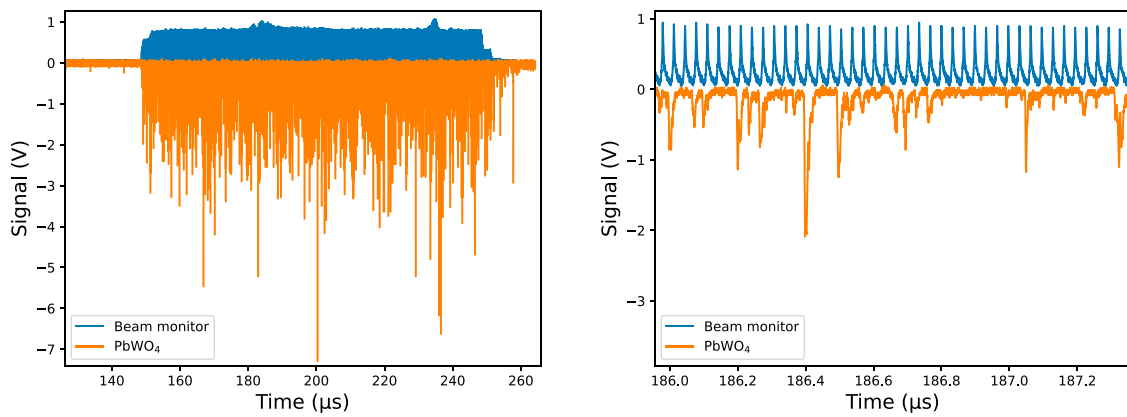
FIGURE 4
Waveforms recorded on the PbWO$_4$ detector and on the fast beam monitor (whose maximum has been normalized to 1 V) for an intensity of 2 µA of the 70 MeV (total energy) alpha particle beam in ARRONAX and a bias voltage of 2500 V. The figure on the right is an enlarged local view.
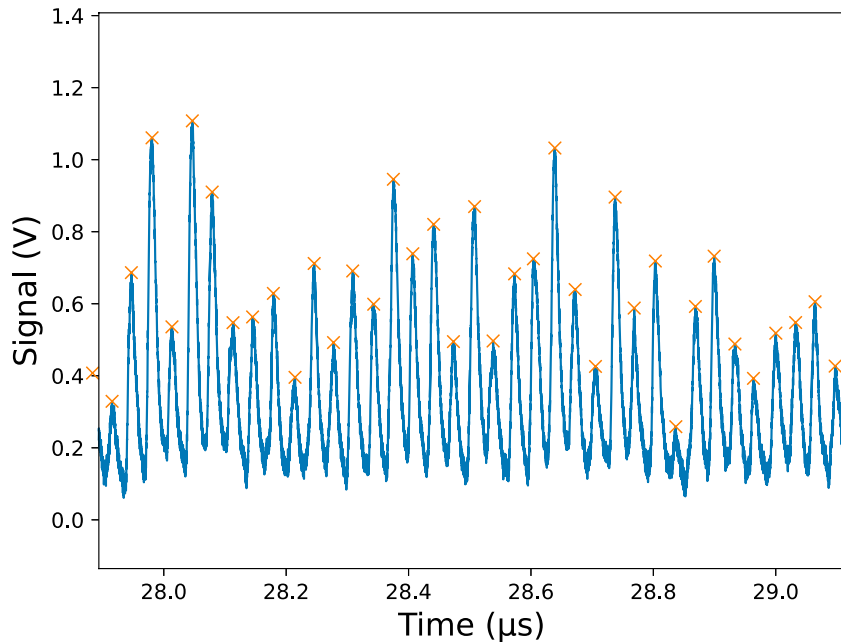
FIGURE 5
Waveforms recorded on the PbWO$_4$ detector for an intensity of 1,600 nA of the 70 MeV (total energy) alpha particle beam in ARRONAX and a bias voltage of 1800 V, displaying the markers provided by the analysis program for identifying individual signals. The waveform has been reversed for the analysis.

The recorded waveforms are then analyzed by a Python script, which initially corrects slight fluctuations in the detectors' baseline (average value subtraction, calculated from the start of the waveform that corresponds to 50 ns without signal). Subsequently, the script performs the integration of the detector signal over the duration of the beam pulse. Various parameters will be explored, such as the evolution of the integral with respect to the incident beam intensity, PMT bias (detector gain), and the distance from the impact point on the target (15 or 25 cm). Moreover, this Python script is able to detect each individual signal within the pulse (Figure 5) to enable correlation between the amplitudes of these

signals and their integrals. The detection of individual signals occurs with the following conditions: a threshold value corresponding to 6 times the standard deviation of the points used for determining the baseline value, a time duration of 2.5 ns above this threshold, and a minimal time separation of 2.5 ns between two consecutive signals. The integral of an individual signal is calculated over a duration of 32.5 ns, 7.5 ns before the local maximum, and the subsequent 25 ns.

The first experiments at CAL and ARRONAX demonstrated a rapid saturation of detectors with high luminosity (NaI and BaF$_2$), when count rates are no longer small compared to the accelerator
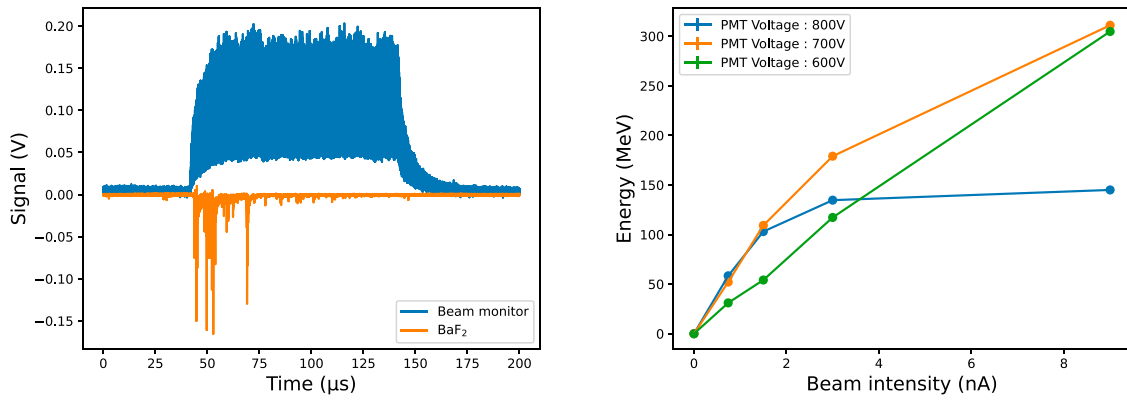
FIGURE 6
Results obtained with NaI(Tl) and BaF$_2$ scintillators placed at 45 cm from the target irradiated with the 68 MeV proton beam in ARRONAX. The pulse duration in 100 µs. Left: waveforms of the beam monitor in blue and the scintillator BaF$_2$ in orange at 3 nA beam intensity; right: evolution of the integral of the waveform during the pulse (expressed in equivalent energy following the detector calibration) on NaI(Tl) *versus* the intensity of the beam for different biases.
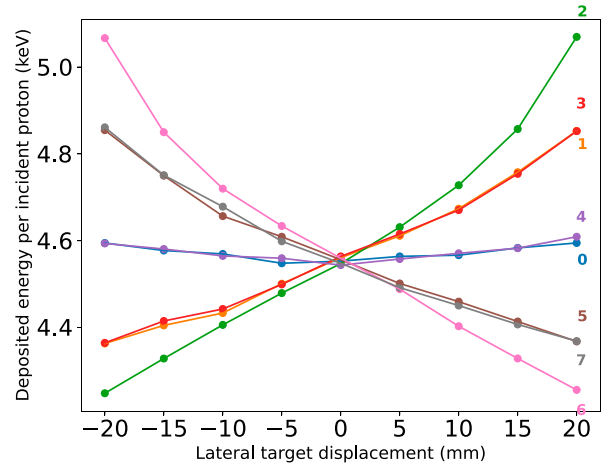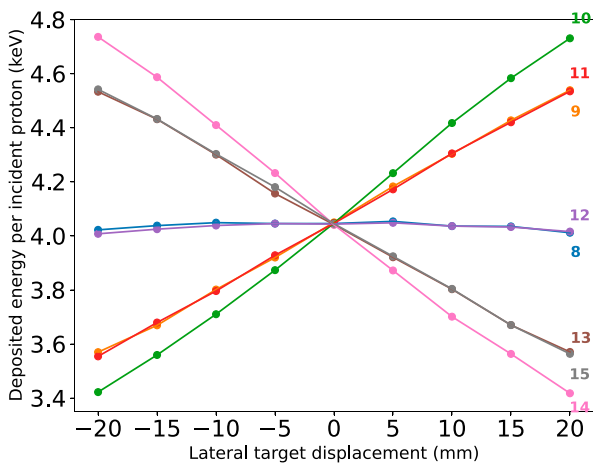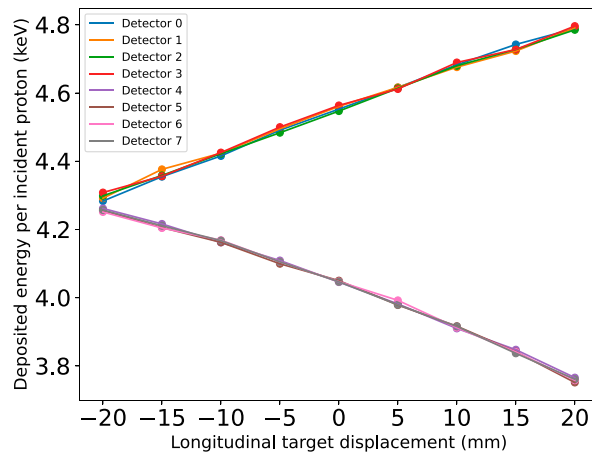
FIGURE 7
Deposited energy (keV) per incident particle (for 10^9 simulated protons) as a function of target displacement in mm. The first figure shows the evolution for longitudinal displacements, the second and the third ones for lateral displacements, with backward and forward detectors, respectively.

FIGURE 8
Expected number of particle detection (PGPI, left) or deposited energy in MeV (PGEI, right) within a group of detectors (forward or backward) for a beam pulse of 1.5×10^7 protons as a function of the target displacement along the incident beam direction. A 1 MeV threshold is applied on particle detection in order discriminate PG that did not interact in the target from background (Compton-scattered PG, electrons, neutrons . . .). The coloured zones correspond to the 1-sigma statistical uncertainty for one measurement.

frequency, as illustrated in Figure 6. In order to avoid detector saturation, a reduction of the PMT bias is necessary to reduce signal amplitudes so that a lower number of PG is expected–with a loss of information–after data analysis based on individual signal detection.

Subsequently, the results will pertain to a scintillator crystal, $PbWO_4$, with a surface area of $4\,cm^2$ and a thickness of 3 cm, coupled with a PMT Photonis-XP2020. $PbWO_4$ was chosen due to its low luminosity (100–300 photons/MeV compared to approximately 38,000 for NaI(Tl)) and rapid scintillation decay constant (6 ns compared to 250 ns for NaI(Tl)), making it an ideal candidate for such applications. Indeed its fast decay time allows it, in principle, to return to its baseline between two consecutive proton pulses separated by 30 ns. However, this low luminosity induces a degraded energy resolution.

3 Results

3.1 Simulations

The simulations allowed for the determination of the evolution of deposited energy based on longitudinal displacements (with 8 detectors in operation) and lateral displacements (with 16 detectors) of the PMMA target. Figure 7 illustrates the obtained results. In each case, a correlation between the target displacement and the energy deposited per incident particle can be observed. In the longitudinal case, two groups of detectors are noticeable—those located upstream from the target (backward) and those located downstream (forward). Within one group, each detector exhibits the same behavior as the others, due to the geometry and symmetry of the setup. Forward detectors (numbered from 0 to 3) experience an increase in deposited energy as the target approaches them, due to the increase of their solid angle relative to the PG emission points. The situation is reversed for backward detectors.

Similarly, the observed variation during lateral displacement is attributed to the variation in the solid angle of the detectors relative

to the emission points. However, other effects contribute to this variation, including the thickness in materials that secondary particles must traverse to reach the detectors. Additionally, the target displacement leads to a modification of the beam entry point and thus the depth of the Bragg peak, resulting in a parabolic evolution of the detected energy in forward detectors for large target displacements. Similar to the longitudinal displacement, symmetries are also clearly seen, explaining the similar evolution of detector pairs, for example, [0,4] [1, 3], and [5, 7] for forward detectors.

The relatively large number of simulated incident ions (10^9) allows for the modeling of a certain number of beam pulses containing a specific quantity of protons. One may add the responses of backward detectors on one hand, and those located forward on the other hand, to detect longitudinal displacement. This increases the perceived statistics as well as precision by a factor $\sqrt{N}$, with N being the number of detectors in the group. Figure 8 illustrates the evolution of the total number of detected particles (left) and the total energy deposition (right) in all detectors of each group for one given pulse of 1.5×10^7 incident protons.

A quasi-linear behaviour is observed (mainly due to the observation angle). The sensitivity of each method is obtained by the ratio between the standard deviation of the simulated statistics and the slope of the linear adjustment function. In this way, the sensitivity to displacement along the beam axis using the PGPI method was calculated to be 1.3 mm at 1σ, while that of the PGEI is 3 mm at 1σ.

3.2 Experiments

The experiments carried out at ARRONAX allowed us to obtain the evolution of the response of a $PbWO_4$ scintillator coupled with a PMT XP2020 (from Photonis) as a function of the incident beam intensity and the PMT bias, for two distances
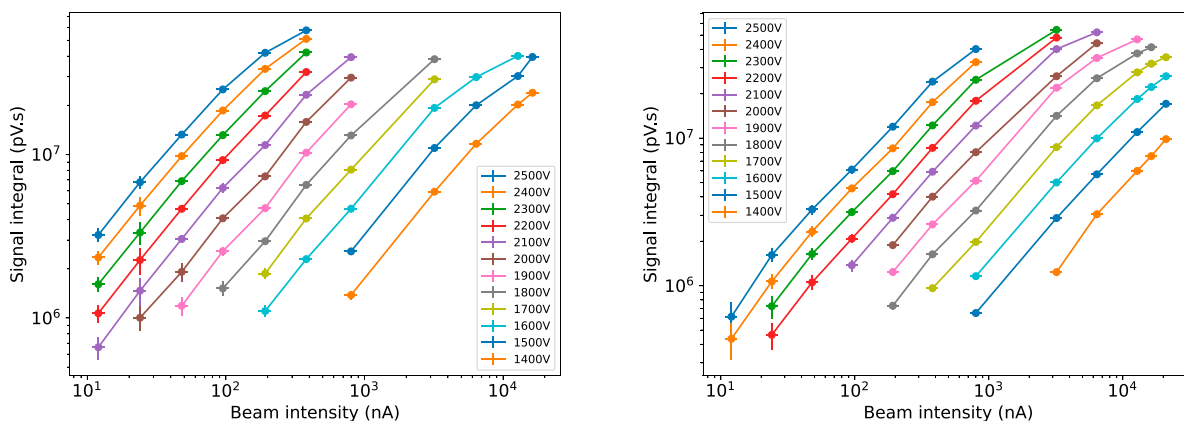
FIGURE 9
Integrals per beam pulse of the ARRONAX accelerator obtained with the PbWO$_4$ detector as a function of 70 MeV proton beam intensity (from 12 nA to almost 21 µA), for the various PMT bias values and 2 distances between the target entrance and the detectors: 15 cm (left) and 25 cm (right).
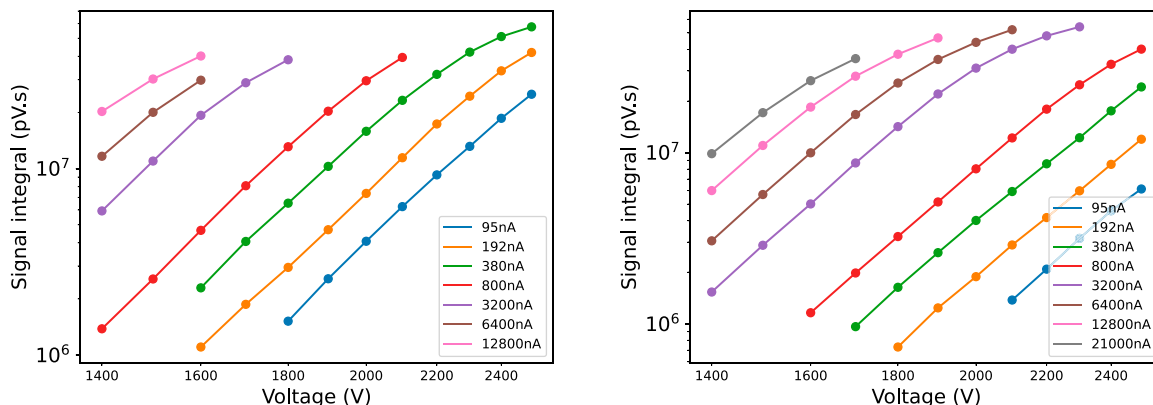
FIGURE 10
Integrals of the recorded waveforms at ARRONAX, with a proton beam of 68 MeV, as a function of the biases applied to the detector and 2 distances between the target entrance and the detectors: 15 cm (left) and 25 cm (right). The different curves correspond to different chosen intensities.

between the entry point of the target and the detector: 15 and 25 cm (Figure 9). First, these experiments show that for each bias value, the integral evolves linearly with the beam intensity until reaching a saturation value (close to 5×10^7 pV·s), at which loss of linearity is seen; the loading charge of the PMT becomes too high. Lowering the bias voltage, and thus reducing the PMT gain, helps to overcome this saturation. Second, as expected, increasing the distance between the detector and the source reduces the detector counting rate, and thus increases the useable range of beam intensity. This is due to the decrease of the detector solid angle: we could check that the count rate ratios are approximately equal to $(15/25)^2$ (the square of the ratio of "target center-detectors" distances) for a given bias in the linear response regime.

These results can also be compared to the documentation from the manufacturer of the PMT XP2020, which provides the characteristic evolution of gain as a function of the bias voltage. By plotting the evolution of the integral of signals against the applied bias, as shown in Figure 10, lines with the same slopes as those in the literature are obtained. The saturation configurations

of the detector also appear in these figures; indeed, there is a noticeable inflection in all curves beyond an integral value of approximately 2×10^7 pV·s.

An example of correlating the amplitudes of individual signals with their integrals is illustrated with density maps shown in Figure 11. These results correspond to a PMT bias of 2000 V for a distance of 25 cm between the target and the detector and a beam intensity of 380 nA (left) and 3,200 nA (right). These results reveal a clear correlation between the signal amplitudes and their integrals. At 380 nA (left figure), saturation is observed for signals above 1.6 V, which is due to the oscilloscope's acquisition window and pertains to only a small number of signals. Moreover, although the two acquisitions presented in Figure 11 correspond to beam intensities different by almost one order of magnitude, there is no indication for detector saturation, as the correlation is maintained. Furthermore, it can be observed that the increase in intensity leads to both an increase in the amplitude of each signal and its integral. In this experimental configuration, the
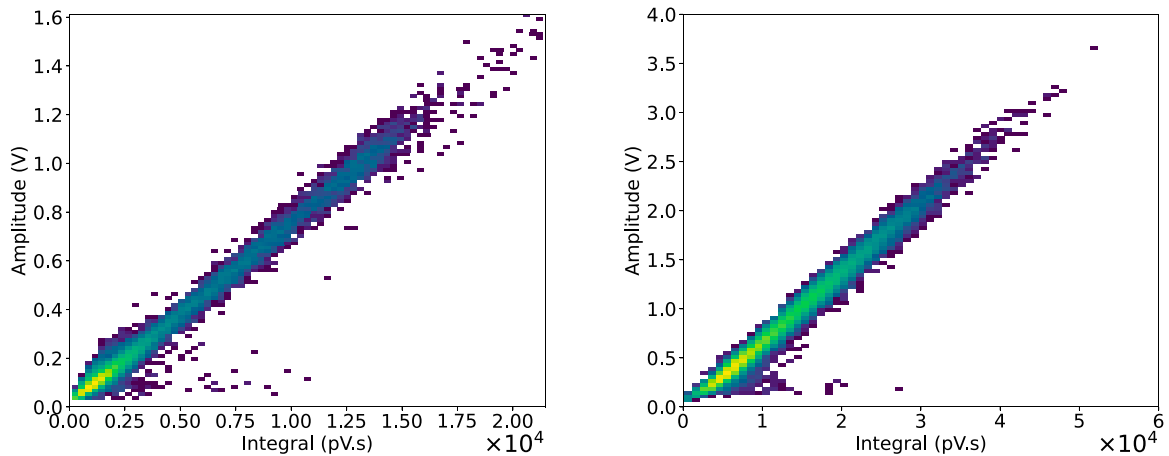
FIGURE 11
Density map of the amplitudes of the individual signals as a function of their integrals for a bias of 2000 V, with the detector placed at a distance of 25 cm from the target entrance and 68 MeV proton beam intensities of 380 nA (left) and 3,200 nA (right).
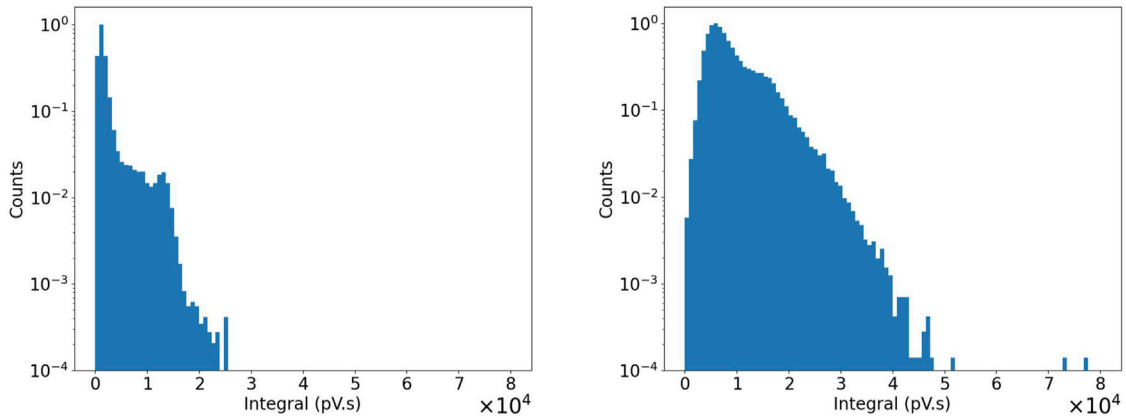
FIGURE 12
Histograms of individual signal integrals for intensities of 380 nA and 3,200 nA with the detector placed at a distance of 25 cm from the target entrance.

duration of pulses are about 3–4 ns, and they are separated by 33 ns (HF period). Therefore, photons detected from the same pulse do lead to both added amplitudes and added signal integrals.

These results are confirmed by the histograms of the integrals of each of these individual signals, which are presented in Figure 12. The spread of the spectrum of integrals at high intensity can be seen in comparison with the lowest intensity.

4 Discussion

4.1 Simulations

The conducted simulations demonstrated that each of the PGPI and PGEI methods is sensitive to the displacement of a target along either the incident beam direction or a transverse axis. Furthermore, it has been shown that the sensitivity obtained from both methods is of the order of a few millimeters with 1.5×10^7 incident protons, positioning these techniques competitively compared to other PG detection methods in the context of online monitoring in hadron therapy [9]. The degradation observed between these two methods arises from two factors. First, the absence of any filter for the PGEI method leads to the necessity of accounting for the contribution induced by neutrons and all other secondaries during irradiation, which carries less precise information about the ion path. Second, even if one considers only prompt-gamma rays, the PGEI method undergoes degradation compared to the PGPI method due to the wide energy spectrum of prompt-gamma rays, ranging from 1 to 10 MeV with an average located at 2 MeV. This leads to a broad dispersion of the averaged sums when multiple photons are detected during a beam pulse (total energies are of the order of 10^5 MeV in Figure 8). Additionally, the sensitivity of each of

these two methods increases with the expansion of the detection zones or the number of detectors around the target.

4.2 Experiments

This experiment demonstrated that the $PbWO_4$ crystal used, with a surface area of 4 cm^2 and a thickness of 3 cm, coupled with an XP2020 PMT, is capable, in certain configurations, to withstand a significant deposited energy flux without saturating the readout system. Thanks to the system performance, we were able to use the same peak intensities as those employed in clinical settings with pulsed beams from clinical synchro-cyclotron accelerators, or even much higher intensities, making the use of the PGEI method feasible for online monitoring in hadron therapy. The crystal used in these characterizations has an equivalent depth but a much smaller surface area than those used in the simulations. In the best case, this detector represents a solid angle about 10 times smaller than that of a detector used in simulations. However, this detector keeps a linear response at high beam intensities, well above the maximum intensity of the considered synchro-cyclotron. It may therefore be possible to increase its solid angle, with a limit of detector saturation at 1 µA. This increase could be accompanied by an expansion of the solid angle by increasing the detection surface. Nevertheless, it is worth noting that a technological constraint on the size of $PbWO_4$ crystals may arise, requiring an increase in the number of detectors in the device to enhance its solid angle.

Furthermore, the development of this method will make use of a dedicated electronic system capable of integrating the signal from each detector. In practice, these signals will be compared to predictions by simulations associated to treatment plans to deduce any potential discrepancies.

4.3 Towards clinical implementation

The simulations were performed with large-sized detectors (cylindrical with a radius of 5 cm). These surface areas are exaggerated but can partly be compensated by increasing the depth of the crystals, which has been set here at 2.5 cm. Indeed, this depth corresponds to a 35% probability of absorption of a 4 MeV photon for $LaBr_3$. Increasing this depth could be a way to compensate for the reduction in surface area. Finally, the application context of these techniques, particularly the PGEI, with pulsed and high-intensity beams offered by synchro-cyclotrons, leads to large loading charge to each detection channel. Therefore, the choice of the scintillation crystal is of crucial importance. The sensitivity of the technique must be studied with realistic simulation of patient treatments. Since MC simulations are not able to thoroughly model all background sources, an additional background level based on experimental measurements can be *a posteriori* added as proposed in [40, 41]. These realistic simulations will allow us to estimate false negatives due to a compensation of different variations (e.g., combined variation in tissue composition and in beam energy) and false positives due to wrong or outdated calibrations (geometry, radiation damage).

The proposed PGEI method has some pros and cons with respect to other range verification methods envisaged for pulsed-particle beam therapy. The detection setup should be compact, like for iono-acoustic [35, 36], electric-field [32] and magnetic field [33, 34] detection. The short-lived beta + emission detection [6] is less compact, but corresponds to a more mature technology. Iono-acoustic detection is an integral method, restricted to soft tissues (without bone barrier). Electric field measurement is an integral method that faces the issue of very low signal, and its feasibility has not been demonstrated yet. Magnetic field measurements are also an integral method, the expected signals are very low and may be perturbed by the environment (beam HF, magnets). The short-lived beta + annihilation detection faces the issue of low statistics at the spot scale for real time verification, and, relative to in-beam PET, the long positron range of beta + emitters like ^{12}N blurs the signal.

Last, the present feasibility study has been intentionally performed using a phantom target with simple geometry, and homogeneous chemical composition. The next step will consist of more realistic studies using several real-size detectors and more complex (anthropomorphic) phantoms irradiated under clinical conditions, in order to compare PGEI measurements with corresponding Monte Carlo simulations. Ideally, a clinical-routine system should be compliant with the (possibly rotating) nozzle and the patient positioning couch. Therefore, a flexible design should be envisaged, depending on the treatment type.

5 Conclusion

This simulation and experimental work brings together the preliminary bricks showing the feasibility of a new prompt-gamma detection technique for particle therapy, adapted to the particular beam delivery conditions of synchro-cyclotrons. The Prompt Gamma Energy Integration (PGEI) is designed to withstand the high counting rates of secondary particles from such accelerators, due to their low duty cycle, and therefore very high peak intensity. Simulations have demonstrated the feasibility of this technique by showing millimetric sensitivity to the displacement of a target along a longitudinal axis for 10^7 protons, corresponding to a single spot of a pencil-beam scanning treatment. Although the background source from scattered particles like neutrons cannot be filtered, unlike PGPI when ToF is measured, the integral energy information makes it possible to reach this performance also with a reduced number of detectors located around the patient. To withstand these high counting rates, it is crucial to choose an appropriate detection system. Characterizations performed on a $PbWO_4$ scintillator have shown a large dynamic range of linear response. This dynamic range extends from the lowest beam intensities to intensities higher than those currently used in clinical practice. This confirms the choice of this detection system and opens up the possibility of monitoring for FLASH-type particle therapy.

Data availability statement

The raw data supporting the conclusion of this article will be made available by the authors, without undue reservation.

Author contributions

PE: Conceptualization, Data curation, Formal Analysis, Investigation, Methodology, Software, Validation, Writing–original draft, Writing–review and editing. DD: Conceptualization, Investigation, Project administration, Supervision, Validation, Writing–review and editing. M-LG-M: Funding acquisition, Investigation, Methodology, Project administration, Resources, Supervision, Validation, Writing–review and editing. JH: Conceptualization, Investigation, Methodology, Resources, Validation, Writing–review and editing. AK: Data curation, Formal Analysis, Investigation, Software, Writing–original draft. CK: Investigation, Methodology, Resources, Validation, Writing–review and editing. JL: Conceptualization, Data curation, Investigation, Methodology, Software, Supervision, Validation, Writing–review and editing. ET: Conceptualization, Data curation, Methodology, Software, Supervision, Validation, Writing–review and editing.

Funding

Acknowledgments

Conflict of interest

The authors declare that the research was conducted in the absence of any commercial or financial relationships that could be construed as a potential conflict of interest.

Publisher's note

All claims expressed in this article are solely those of the authors and do not necessarily represent those of their affiliated organizations, or those of the publisher, the editors and the reviewers. Any product that may be evaluated in this article, or claim that may be made by its manufacturer, is not guaranteed or endorsed by the publisher.

References

1. Durante M, Paganetti H. Nuclear physics in particle therapy: a review. *Rep Prog Phys* (2016) 79:096702. Physical Society (Great Britain). doi:10.1088/0034-4885/79/9/096702

2. Knopf AC, Lomax A. *In vivo* proton range verification: a review. *Phys Med Biol* (2013) 58:131–60. doi:10.1088/0031-9155/58/15/R131

3. Paganetti H. Range uncertainties in proton therapy and the role of Monte Carlo simulations. *Phys Med Biol* (2012) 57:R99–R117. doi:10.1088/0031-9155/57/11/R99

4. Parodi K, Bortfeld T, Enghardt W, Fiedler F, Knopf A, Paganetti H, et al. PET imaging for treatment verification of ion therapy: implementation and experience at GSI Darmstadt and MGH Boston. *Nucl Instr Methods Phys Res Section A: Acc Spectrometers, Detectors Associated Equipment* (2008) 591:282–6. doi:10.1016/j.nima.2008.03.075

5. Bisogni MG, Attili A, Battistoni G, Belcari N, Camarlinghi N, Cerello P, et al. INSIDE in-beam positron emission tomography system for particle range monitoring in hadrontherapy. *J Med Imaging* (2016) 4:011005. doi:10.1117/1.JMI.4.1.011005

6. Dendooven P, Buitenhuis HJT, Diblen F, Heeres PN, Biegun AK, Fiedler F, et al. Short-lived positron emitters in beam-on PET imaging during proton therapy. *Phys Med Biol* (2015) 60:8923–47. doi:10.1088/0031-9155/60/23/8923

7. Tashima H, Yoshida E, Inadama N, Nishikido F, Nakajima Y, Wakizaka H, et al. Development of a small single-ring OpenPET prototype with a novel transformable architecture. *Phys Med Biol* (2016) 61:1795–809. doi:10.1088/0031-9155/61/4/1795

8. Paganetti H, El Fakhri G. Monitoring proton therapy with pet. *Br J Radiol* (2015) 88:20150173. doi:10.1259/bjr.20150173

9. Krimmer J, Dauvergne D, Létang JM, Testa E. Prompt-gamma monitoring in hadrontherapy: a review. *Nucl Instr Methods Phys Res Section A: Acc Spectrometers, Detectors Associated Equipment* (2018) 878:58–73. doi:10.1016/j.nima.2017.07.063

10. Min CH, Kim CH, Youn MY, Kim JW. Prompt gamma measurements for locating the dose falloff region in the proton therapy. *Appl Phys Lett* (2006) 89. doi:10.1063/1.2378561

11. Testa E, Bajard M, Chevallier M, Dauvergne D, Le Foulher F, Freud N, et al. Monitoring the Bragg peak location of 73 MeVu carbon ions by means of prompt γ-ray measurements. *Appl Phys Lett* (2008) 93. doi:10.1063/1.2975841

12. Verburg JM, Seco J. Proton range verification through prompt gamma-ray spectroscopy. *Phys Med Biol* (2014) 59:7089–106. doi:10.1088/0031-9155/59/23/7089

13. Polf JC, Panthi R, Mackin DS, McCleskey M, Saastamoinen A, Roeder BT, et al. Measurement of characteristic prompt gamma rays emitted from oxygen and carbon in tissue-equivalent samples during proton beam irradiation. *Phys Med Biol* (2013) 58:5821–31. doi:10.1088/0031-9155/58/17/5821

14. Krimmer J, Ley JL, Abellan C, Cachemiche JP, Caponetto L, Chen X, et al. Development of a Compton camera for medical applications based on silicon strip and scintillation detectors. *Nucl Instr Methods Phys Res Section A: Acc Spectrometers, Detectors Associated Equipment* (2015) 787:98–101. doi:10.1016/j.nima.2014.11.042

15. Perali I, Celani A, Bombelli L, Fiorini C, Camera F, Clementel E, et al. Prompt gamma imaging of proton pencil beams at clinical dose rate. *Phys Med Biol* (2014) 59:5849–71. doi:10.1088/0031-9155/59/19/5849

16. Xie Y, Bentefour EH, Janssens G, Smeets J, Vander Stappen F, Hotoiu L, et al. Prompt gamma imaging for *in-vivo* range verification of pencil beam scanning proton therapy. *Int J Radiat Oncol Biol Phys* (2017) 99:210–8. doi:10.1016/j.ijrobp.2017.04.027

17. Krimmer J, Balleyguier L, Baudot J, Brons S, Caponetto L, Chabot M, et al. Real-time online monitoring of the ion range by means of prompt secondary radiations. In: 3rd International Conference On Advancements In Nuclear Instrumentation Measurement Methods And Their Applications (ANIMMA 2013); 23-27 June 2013; Marseille, France (2013). p. 1–8.

18. Kasper J, Rusiecka K, Hetzel R, Kozani MK, Lalik R, Magiera A, et al. The sifi-cc project – feasibility study of a scintillation-fiber-based compton camera for proton therapy monitoring. *Physica Med* (2020) 76:317–25. doi:10.1016/J.EJMP.2020.07.013

19. Liprandi S, Takyu S, Aldawood S, Binder T, Dedes G, Kamada K, et al. Characterization of a compton camera setup with monolithic labr 3 (ce) absorber and segmented gagg scatter detectors. In: 2017 IEEE Nuclear Science Symposium and Medical Imaging Conference, NSS/MIC 2017 - Conference Proceedings; 21-28 October 2017; Atlanta, GA, USA (2018).

20. Taya T, Kataoka J, Kishimoto A, Iwamoto Y, Koide A, Nishio T, et al. First demonstration of real-time gamma imaging by using a handheld compton camera for particle therapy. *Nucl Instr Methods Phys Res Section A: Acc Spectrometers, Detectors Associated Equipment* (2016) 831:355–61. doi:10.1016/J.NIMA.2016.04.028

21. Jiang Z, Polf JC, Barajas CA, Gobbert MK, Ren L. A feasibility study of enhanced prompt gamma imaging for range verification in proton therapy using deep learning. *Phys Med Biol* (2023) 68:075001. doi:10.1088/1361-6560/ACBF9A

22. Viegas R, Roser J, Barrientos L, Borja-Lloret M, Casaña JV, López JG, et al. Characterization of a compton camera based on the tofpet2 asic. *Radiat Phys Chem* (2023) 202:110507. doi:10.1016/J.RADPHYSCHEM.2022.110507

23. Marcatili S, Collot J, Curtoni S, Dauvergne D, Hostachy JY, Koumeir C, et al. Ultra-fast prompt gamma detection in single proton counting regime for range monitoring in particle therapy. *Phys Med Biol* (2020) 65:245033. doi:10.1088/1361-6560/ab7a6c

24. Jacquet M, Ansari S, Gallin-Martel ML, André A, Boursier Y, Dupont M, et al. A high sensitivity cherenkov detector for prompt gamma timing and time imaging. *Scientific Rep* (2023) 13:3609. doi:10.1038/s41598-023-30712-x

25. Golnik C, Hueso-González F, Müller A, Dendooven P, Enghardt W, Fiedler F, et al. Range assessment in particle therapy based on prompt γ-ray timing measurements. *Phys Med Biol* (2014) 59:5399–422. doi:10.1088/0031-9155/59/18/5399

26. Krimmer J, Angellier G, Balleyguier L, Dauvergne D, Freud N, Hérault J, et al. A cost-effective monitoring technique in particle therapy via uncollimated prompt gamma peak integration. *Appl Phys Lett* (2017) 110. doi:10.1063/1.4980103

27. Hueso-Gonzalez F, Bortfeld T. Compact method for proton range verification based on coaxial prompt gamma-ray monitoring: a theoretical study. *IEEE Trans Radiat plasma Med Sci* (2020) 4:170–83. doi:10.1109/TRPMS.2019.2930362

28. Dauvergne D, Allegrini O, Caplan C, Chen X, Curtoni S, Etxebeste A, et al. On the role of single particle irradiation and fast timing for efficient online-control in particle therapy. *Front Phys* (2020) 8:434. doi:10.3389/fphy.2020.567215

29. Jolly S, Owen H, Schippers M, Welsch C. Technical challenges for flash proton therapy. *Physica Med* (2020) 78:71–82. doi:10.1016/j.ejmp.2020.08.005

30. Favaudon V, Caplier L, Monceau V, Pouzoulet F, Sayarath M, Fouillade C, et al. Ultrahigh dose-rate flash irradiation increases the differential response between normal and tumor tissue in mice. *Sci Translational Med* (2014) 6:245ra93. doi:10.1126/scitranslmed.3008973

31. Montay-Gruel P, Corde S, Laissue JA, Bazalova-Carter M. FLASH radiotherapy with photon beams. *Med Phys* (2022) 49:2055–67. doi:10.1002/mp.15222

32. Albert J, Labarbe R, Sterpin E. Electric field from a proton beam in biological tissues for proton radiotherapy. *Phys Rev Appl* (2018) 10:044054. doi:10.1103/PhysRevApplied.10.044054

33. Rädler M, Gianoli C, Palaniappan P, Parodi K, Riboldi M. Electromagnetic signal of a proton beam in biological tissues for a potential range-verification approach in proton therapy. *Phys Rev Appl* (2021) 15:024066. doi:10.1103/PhysRevApplied.15.024066

34. Rädler M, Buizza G, Kawula M, Palaniappan P, Gianoli C, Baroni G, et al. Impact of secondary particles on the magnetic field generated by a proton pencil beam: a finite-element analysis based on Geant4-DNA simulations. *Med Phys* (2023) 50:1000–18. doi:10.1002/mp.16062

35. Hickling S, Xiang L, Jones KC, Parodi K, Assmann W, Avery S, et al. Ionizing radiation-induced acoustics for radiotherapy and diagnostic radiology applications. *Med Phys* (2018) 45:e707–21. doi:10.1002/mp.12929

36. Lascaud J, Dash P, Wieser HP, Kalunga R, Würl M, Assmann W, et al. Investigating the accuracy of co-registered ionoacoustic and ultrasound images in pulsed proton beams. *Phys Med Biol* (2021) 66:185007. doi:10.1088/1361-6560/ac215e

37. Sarrut D, Arbor N, Baudier T, Borys D, Etxebeste A, Fuchs H, et al. The OpenGATE ecosystem for Monte Carlo simulation in medical physics. *Phys Med Biol* (2022) 67:184001. doi:10.1088/1361-6560/ac8c83

38. Allison J, Amako K, Apostolakis J, Arce P, Asai M, Aso T, et al. Recent developments in Geant4. *Nucl Instr Methods Phys Res Section A: Acc Spectrometers, Detectors Associated Equipment* (2016) 835:186–225. doi:10.1016/j.nima.2016.06.125

39. Wrońska A, Kasper J, Ahmed AA, Andres A, Bednarczyk P, Gazdowicz G, et al. Prompt-gamma emission in GEANT4 revisited and confronted with experiment. *Physica Med* (2021) 88:250–61. doi:10.1016/j.ejmp.2021.07.018

40. Pinto M, Dauvergne D, Freud N, Krimmer J, Letang JM, Ray C, et al. Design optimisation of a TOF-based collimated camera prototype for online hadrontherapy monitoring. *Phys Med Biol* (2014) 59:7653–74. doi:10.1088/0031-9155/59/24/7653

41. Huisman BFB, Muñoz E, Dauvergne D, Létang JM, Sarrut D, Testa E. Analytical modeling and Monte Carlo simulations of multi-parallel slit and knife-edge slit prompt gamma cameras. *Phys Med Biol* (2023) 68:115009. doi:10.1088/1361-6560/acd237